Comparison of microstructure changes induced in two pearlitic rail steels subjected to a full-scale wheel/rail contact rig test

J. Wen, J. Marteau, Salima Bouvier, Marion Risbet, F. Cristofari, P. Secordel

Comparison of microstructure changes induced in two pearlitic rail steels subjected to a full-scale wheel/rail contact rig test

J. Wen[1], J. Marteau[2], S. Bouvier[2], M. Risbet[2], F. Cristofari[3], P. Secordel[3]

[1]Technological Research Institute (IRT) Railenium, Technopôle Transalley, 180 rue Joseph-Louis Lagrange, 59308 Valenciennes Cedex, France

[2]Alliance Sorbonne Universités, Université de Technologie de Compiègne, Laboratoire Roberval de Mécanique FRE UTC-CNRS 2012, Centre de Recherche Royallieu - CS 60 319 - 60 203 Compiègne Cedex, France

[3]France Rail Industry, 164 rue du Maréchal-Foch, BP 10166, 57705 Hayange Cedex, France

Abstract

This study focused on the comparison of the microstructure changes induced in two pearlitic rail steels subjected to full-scale wheel-rail contact rig tests (DB Systemtechnik, Germany): a conventional R260 steel grade and a heat-treated premium R370CrHT rail grade (also known as MHH400). The total loading of the wheel/rail contact rig test was computed to be 2.4 million gross tons but aimed at reproducing large deformations caused by loadings around 100 million gross tons into the materials. The description of the microstructure showed the ability of the rig to reproduce large loadings. Through the coupling of optical and SEM observations, EBSD measurements and hardness tests along the depths of the tested rails, it was shown that the plastic deformation was much more confined in R370CrHT than in R260. This thorough comparison of the microstructure changes will help the building of wear scenarios.

Keywords

Steel, rail-wheel tribology, electron microscopy, wear testing.

1. Introduction

Surface damage of rail steels and related costs of inspection and maintenance are important issues for modern railway infrastructures. Moreover, the constant rise of loadings, frequency and speed of trains only intensifies this issue with the increase of the stresses borne by the railways. To limit contact

fatigue and wear, new steel grades have been searched for several years. In the fifties, hypoeutectoid steels (bi-phased ferrite/pearlite steels) were preferred (*e.g.* R220). Then, in the seventies, hardness increase was looked for to limit fatigue contact and wear. This resulted in the increase of carbon content and thus the development of eutectoid steels such as R260. From the eighties, the mechanical properties of rail steels were further improved with the development of thermal treatments (*e.g.* R350HT) and the use of selective alloying (*e.g.* R370CrHT). These developments were conducted concurrently with the examination of the resistance of these materials to wear and fatigue. Currently, the main known metallurgical factors contributing to the wear and fatigue resistance of pearlitic steels are: solid solution hardening, the size of pearlite colonies [1], the interlamellar spacing [2] and the size of prior austenite grains [3].

To investigate the behavior of rails subjected to rolling contact, microstructural analysis is often performed before and after their loading using optical microscope observations coupled with hardness tests [4,5]. Scanning Electron Microscopy (SEM) is an increasingly favored method of observation [6,7]. However, the microstructure descriptions tend to remain qualitative rather than quantitative (*e.g.* the description of colony orientation [8,9]), with the exception of the interlamellar spacing [10]. A quantitative description of the microstructure of pearlitic steels remains little addressed due to its complexity and its large cost in terms of analysis and measuring time. The use of the Electron BackScattering Diffraction (EBSD) technique is slowly growing for the characterization of the microstructure of pearlitic steels [11,12]. More recently, Linz *et al.* [13] investigated the early damage phenomena taking place in R260 steel by coupling SEM, EBSD and hardness results. Similarly, Dylewski *et al.* [14] used a multiscale analysis to examine head check initiation in R260 steel.

As underlined by Pointner [15], despite the numerous studies, the relationship between the features of the microstructure of grade steels and mechanical contact or more particularly the resistance to wear and fatigue is not clearly established yet.

Based on these observations, the study presented hereafter focused on the comparison of the microstructure changes induced in two pearlitic rail steels subjected to full-scale wheel-rail contact rig tests (DB Systemtechnik, Germany). The coupling of optical and SEM observations, EBSD measurements and hardness tests along the depths of the tested rails were used to investigate the

plastic deformation differences between a conventional R260 steel grade and a heat-treated premium R370CrHT rail grade (also known as MHH400) at the scale of the microstructure.

	C	Si	Mn	P max.	S max.	Cr	Al max.	V max.	N max.
R220	0.50/0.60	0.20/0.60	1.00/1.25	0.025	0.025	0.15 max.	0.004	0.030	0.010
R260*	0.60/0.82	0.13/0.60	0.65/1.25	0.030	0.030	0.15 max.	0.004	0.030	0.010
R350HT	0.70/0.82	0.13/0.60	0.65/1.25	0.025	0.030	0.15 max.	0.004	0.030	0.010
R370CrHT*	0.70/0.82	0.40/1	0.70/1.10	0.020	0.020	0.40/0.60	0.004	0.030	0.010

Table 1: Composition of the discussed grade rails (weight %), according to [16]. The steels examined in this paper are indicated using a mark (*).

2. Materials and methods

2.1. Rail material and test rig conditions

Two pearlitic steel grades were tested: R260 and R370CrHT improved to achieve 400 HB on the surface (also known as MHH400). Their chemical compositions are presented in Table 1. One rail made from each pearlitic steel grade was tested. Both rails had a 60E2 profile (thus a section of 76.48 cm²) and a total length of 3.2 m. The rail segments were subjected to 100,000 load cycles using a full scale linear test rig (DB Systemtechnik, Germany) with a static contact force of 120 kN, a lateral force of 10 kN and a rolling contact length of 2 m. Each test lasted approximately 4 days. The forces were only applied during forward motion. The wheel was completely raised from the rail during the reverse motion so that the testing scenario corresponded to a rolling in a single direction. An angle of attack of 3 mrad was used to simulate the testing conditions of curve negotiation. Monoblock wheels made of ER8 steel with a S1002 profile were used for the tests, in accordance with [17]. The total load of the rail was approximately equal to 2.4 million gross tons (MGT) but it aimed at simulating an equivalent on-track loading of 100 MGT.

2.2. Measurements

2.2.1. Microstructure analysis

Specimens of 10 x 10 mm² were cut from the tested rails. The specimens were taken from the area located 5 mm from the symmetrical axis of the rail head either in the worn part or in the non-deformed part of the rail. Microstructures were characterized using a field emission gun– scanning electron microscope (Σigma™, Zeiss, Germany) equipped with a EBSD detector (OptiPlex 7040, Nordif, Norway). EBSD measurements were performed with an accelerating voltage of 25 kV, a tilt of 70° and a working distance of 20 mm. Different measurement step sizes were chosen depending on the required resolutions for the investigations: 500 nm for nodule characterization and 100 nm for assessing local plastic deformation. Orientation maps were calculated with TSL OIM data collection™ software [18].

The specimens cut from the rails were polished using successive abrasive SiC papers (P300, P500, P1000, P2000 and P4000) to remove the oxidized and contaminated layers. Then, the samples were polished with 3 µm, 1 µm diamond solution and OPS solution respectively for 10 min, 8 min and 5 min. For EBSD measurements, the specimens were polished with 10% oxide polishing suspension solution and 90% of H_2O in Buehler VibroMet™ 2 vibratory polisher for three days. For Optical Microscopy (OM) observation, chemical attack in 1% Nital solution for 5 seconds was employed.

2.2.2. Wear and microhardness

After the wheel/rail tests, measurements of the rail profiles using a MiniProf profilometer were performed to determine the transverse profile and the corresponding wear depths. Micro-hardness measurements were performed with a Vickers indenter using a LECO M-400 micro-hardness tester with a load of 300 gf (HV0.3). The indentation tests were achieved on the cross-section of the specimens with a distance between two indents equal to four times the mean indentation length. Three lines of tests were completed on each examined cross-section.

3. Results and discussion

3.1. Macroscopic observations

The cyclic stresses caused by the contact between wheel and rail entailed significant changes in the rail profiles. Figure 1a presents the average values of rail profiles for R260 and R370CrHT after the rolling contact wheel/rail test with a total load approximately equal to 2.4 MGT, as well as a 60E2 reference profile. The loss of transverse rail profile was more severe in R260 than in R370CrHT.

Based on the profile shapes, the wear depth was estimated to be around 0.8 mm for R260 while it was equal to 0.2 mm for R370CrHT.

It is worth noting that a series of OM observations along the rail profiles (Figure 1b, c and d) also showed that headchecks took place in the R260 rail while no headchecks were detected in the R370CrHT rail. This piece of information underlines the bench ability of reproducing effects caused by curve negotiation.

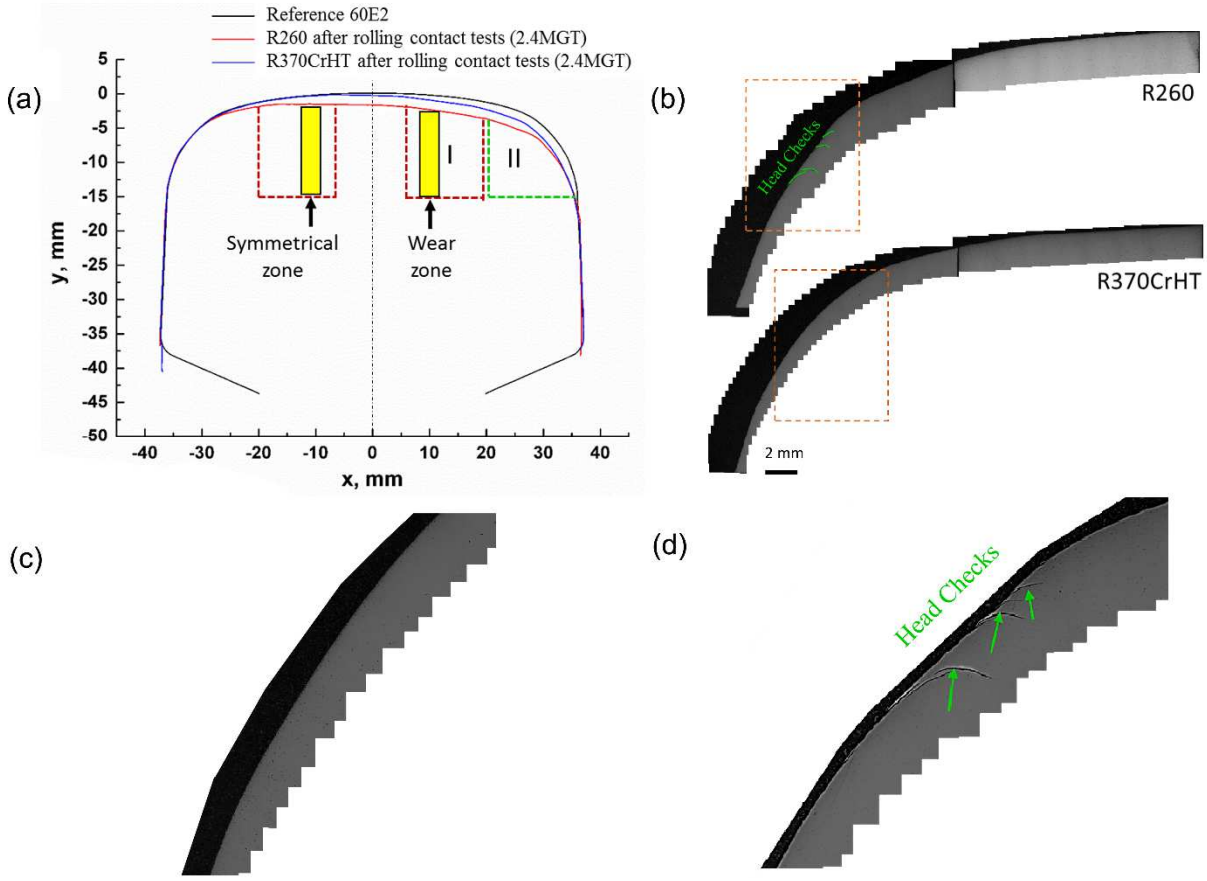

Figure 1: (a) Profiles of rails after rolling contact wheel/rail rig testing and reference profile for 60E2; (b) OM observations of the wear and head check zones in the cross section of two rails, (c) magnified OM figure for R370CrHT and (d) magnified OM figure for R260.

3.2. Microscopic observations

Hereafter, the presented results will focus on the wear zone schematically depicted in Figure 1a. The evolution of the microstructure of this area will be compared to the area called 'symmetrical zone' underlined in Figure 1a. The symmetrical area was chosen as reference for the microstructure characterization because it does not undergo any deformation during the test. A closer examination of Figure 1a shows a slight loss of profile in the symmetrical zone compared to the reference line but it

was caused by grinding prior to the rolling contact test. It should be noted that the field corner of rails is often chosen as the reference instead of the symmetrical zone. However, such a choice would not be relevant for this study because the examined R370CrHT steel underwent thermal treatment that led to the development of different microstructure characteristics in the field corner and symmetrical zone.

3.2.1. Initial state

Both materials had a pearlite microstructure composed of alternating lamellae of ferrite and cementite phases (as underlined in Figure 2a). As the interlamellar spacing S_p is known to play a crucial role in the yield strength and hardness of pearlite steel, it was quantified in both materials. Two hundred fifty measurements were performed across straight lamellae groups, as illustrated in Figure 2a and b. These measurements were performed at different depths to get an average value of S_p for the undeformed areas. The average interlamellar spacing of R260 was identified to be equal to 310 ± 20 nm while it was equal to 73 ± 5 nm for R370CrHT. Thus, the average interlamellar spacing was approximately four times larger in R260 than in R370CrHT.

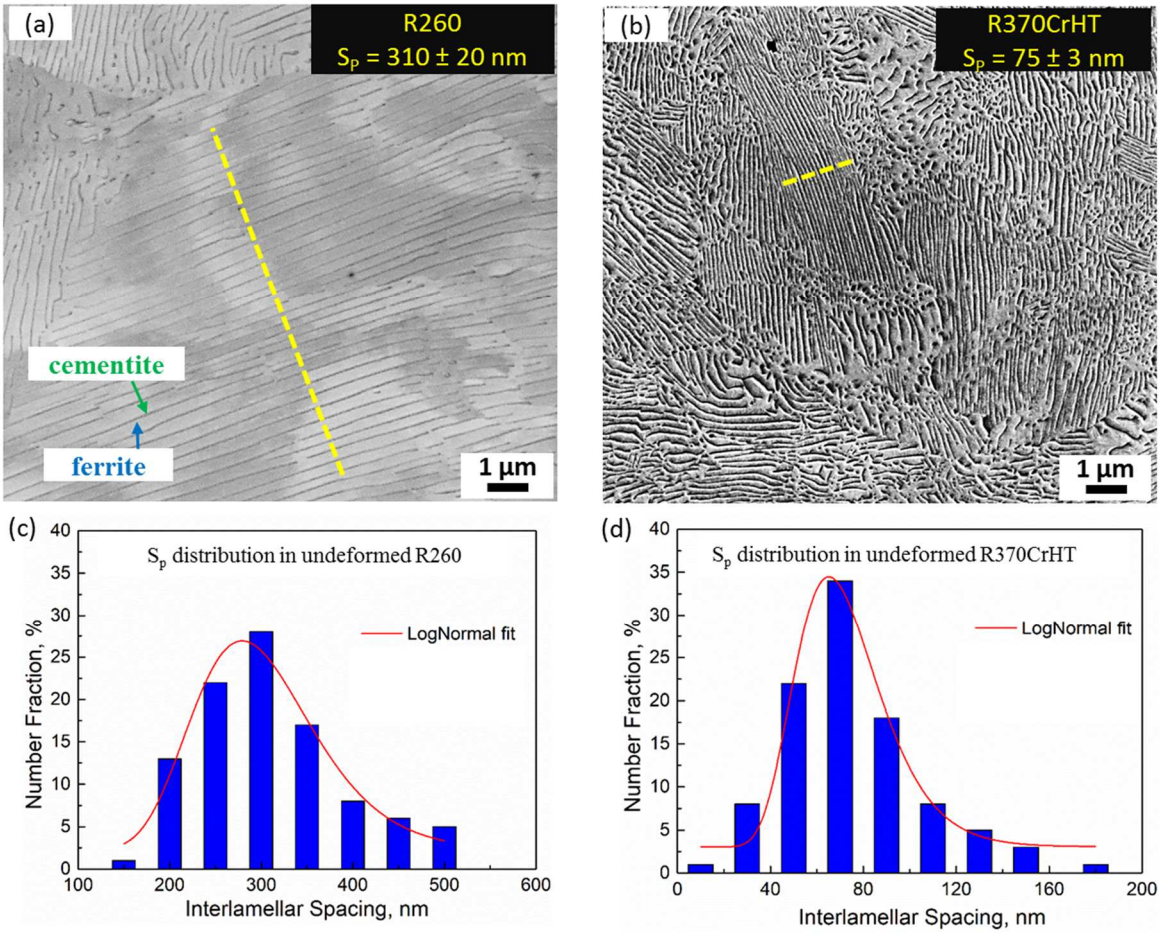

Figure 2: SEM images of typical pearlite microstructure for the undeformed (a) R260 and (b) R370CrHT rail grades with examples of determination of interlamellar spacing (S_P) and the computed distribution of interlamellar spacing for (c) R260 and (d) R370CrHT. Cementite and ferrite lamellae are indicated by green and blue arrow in (a).

Then, microstructure characterization of the unloaded area of the rails was performed using SEM-EBSD measurements. First, large EBSD maps with a step size of 500 nm were performed in the symmetrical zone, near the surface, to quantify the nodule size. Nodules were defined as regions separated by misorientation angles larger than 10°. Figure 3a and b shows the Inverse Pole Figures (IPF) obtained in the symmetrical area of the worn rail samples, near the surface, for R260 and R370CrHT, respectively. The nodule size was found to be around 37 µm ± 29 µm for R260 and 25 ± 14 µm for R370CrHT. Despite the large standard deviations, these computations showed that R260 had larger nodule sizes than R370CrHT and that the nodule sizes were more spread (the coefficient of variation was equal to 0.78 for R260 and 0.56 for R370CrHT). Based on these large EBSD maps, pole figures were also drawn. For the sake of brevity these figures were not included but no preferential orientation of pearlite was observed for both R260 and R370CrHT with respect to the rolling direction. Thus, no texture developed in the near surface of the railheads during the production of the rails. Figure 4 shows the results of finer EBSD scans with a step size of 100 nm in the same region. IPF maps were superimposed with Image Quality (IQ) results and IQ map with the values of the rotation angles. For R260, as the interlamellar spacing is larger than the EBSD step size, the lamellar microstructure clearly appeared on the combined IPF and IQ maps. On the opposite, for R370CrHT, the interlamellar spacing is too small compared to the EBSD step to give a clear definition of the lamellae. For the selected areas, a total length of boundaries of 1.2 mm was measured for R260 with 64% of Low Angle Boundaries (LAB) i.e. boundaries with rotation angles comprised between 2 and 10 degrees and 36% of High Angle Boundaries (HAB) i.e. boundaries with rotation angles comprised between 10 and 65 degrees. For R370CrHT, a total length of boundaries of 2.3 mm was measured for an equal size of zone, composed of 60 % of LAB and 40% for HAB. These computations were repeated on several areas. The difference of total length of boundaries between R260 and R370CrHT was significant and can be explained by the finer nodule and colony structure of R370CrHT compared to R260.

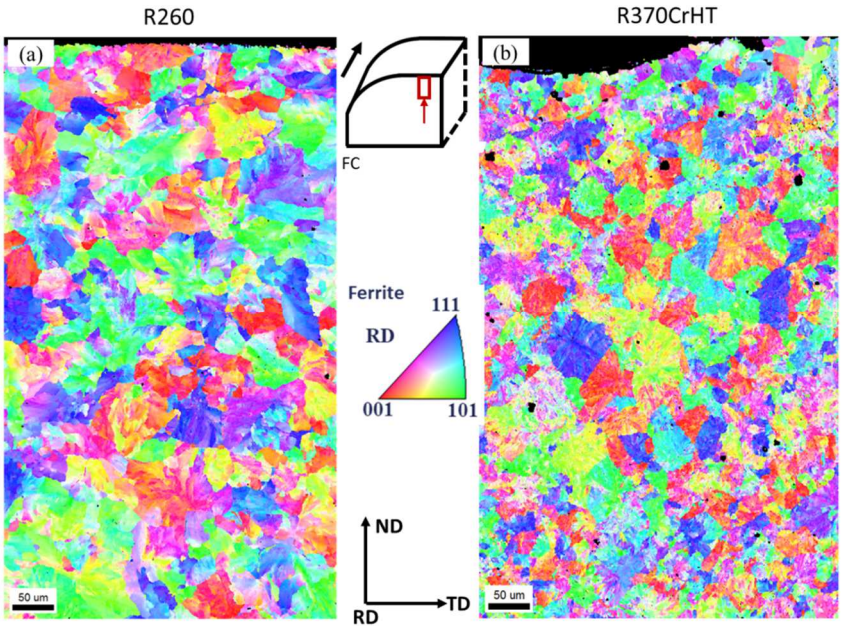

Figure 3: EBSD characterization of the undeformed zone (symmetrical area) in the worn rail samples with a step of 500 nm: IPF of (a) R260 and (b) R370CrHT.

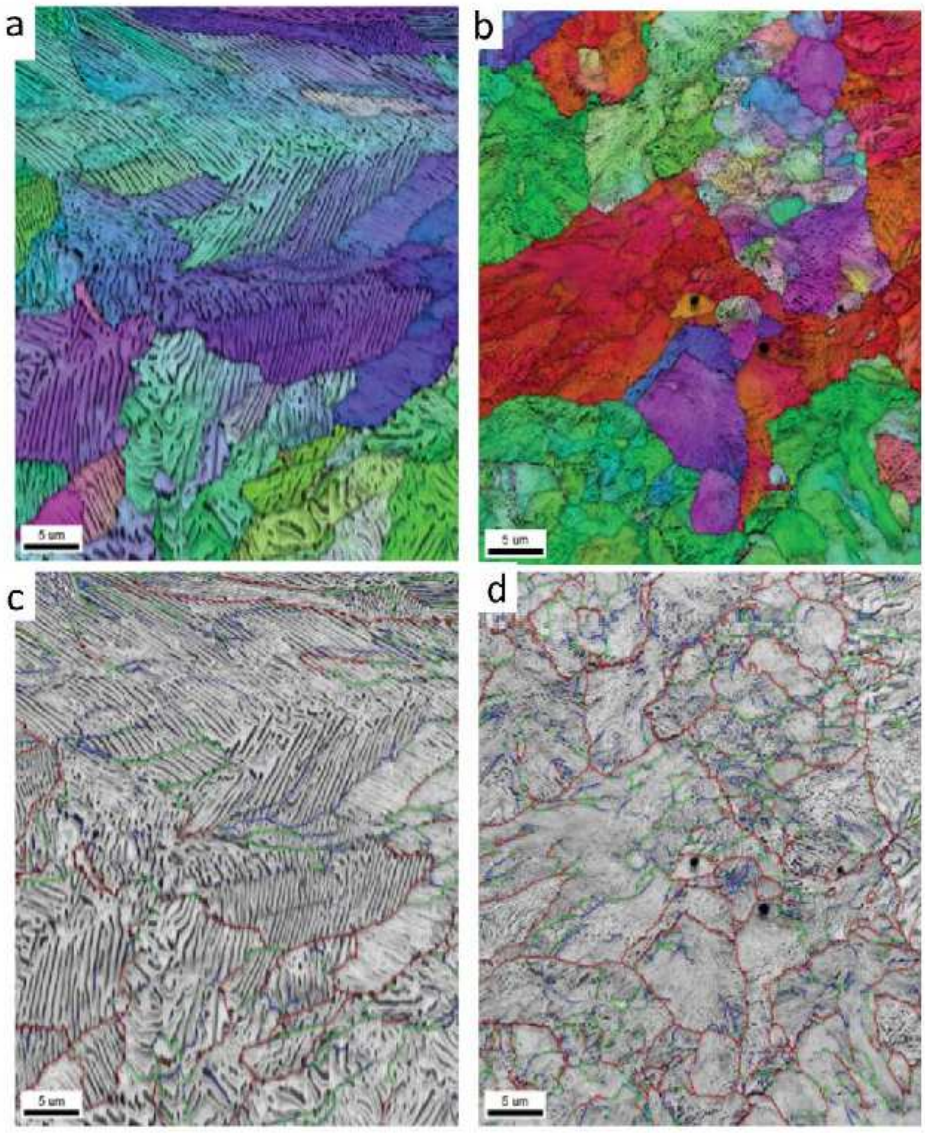

Figure 4: EBSD characterizations performed at a depth of 4000 µm in the symmetry zone with a step size of 100 nm: IPF maps superimposed with image quality of (a) R260, (b) R370CrHT and IQ maps with grain boundaries (2-5° in blue, 5-10° in green, 15-65° in red) for (c) R260 and (d) R370CrHT.

3.2.2. Worn state

First, the evolution of interlamellar spacing S_p and hardness was determined as a function of the rail depth (Figure 5). The interlamellar spacing was quantified with a statistical analysis of SEM images for both materials. Near the material surface, S_p fell by around 50% for R260 if compared to the value found in the symmetrical area while S_p only fell by around 20 % for R370CrHT. Furthermore, for R260, S_p gradually increased from the surface of the material down to a depth of approximately 1500 µm, while for R370CrHT there was a steep increase until a depth of only 350 µm. It should be noted that after these brutal variations caused by the material deformation, both materials showed a slight

increase of S_p with depth, instead of reaching a plateau. This slight increase results from the different cooling rates of the material during the steelmaking process. Microindentation tests were also performed on the cross-section of both materials. Figure 5b presents the variation of the microhardness divided by the microhardness determined before loading, as a function of depth. An increase of the microhardness of 60% at the surface of the material was observed for R260 while this increase was only of 30% for R370CrHT. The microhardness of R260 gradually decreased until a depth of approximately 600 µm while the microhardness of R370CrHT quickly decreased over a depth of around 350 µm. It should be noted that the interlamellar spacing and the microhardness varied over similar depths for R370CrHT. On the opposite, for R260, the variation depth of the interlamellar spacing took place over around twice the distance determined for the microhardness.

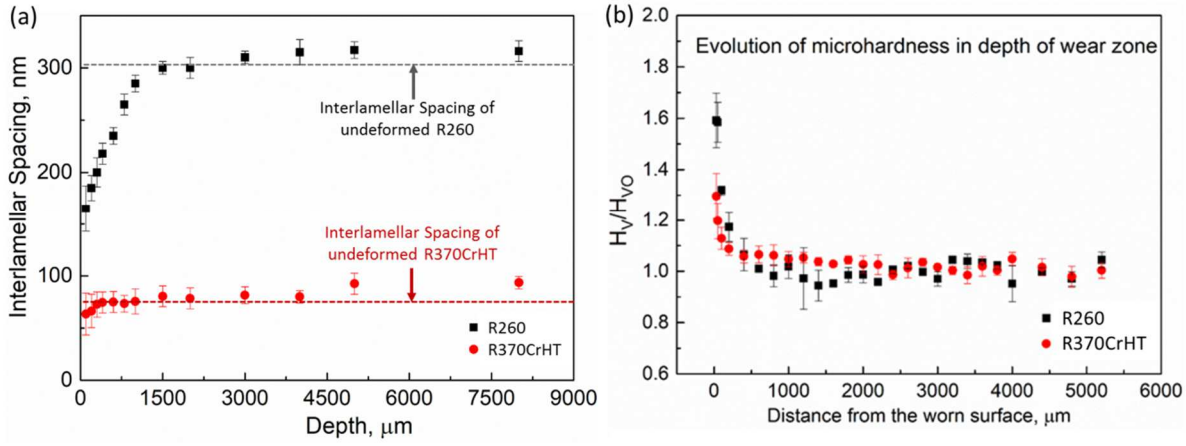

Figure 5: Variation of interlamellar spacing S_p (a) and microhardness $H_V/H_{V(undeformed)}$ (b) with the distance from the worn surface in R260 and R370CrHT after rolling contact tests.

Figure 6 shows the SEM-EBSD characterization of the microstructure directly below the worn surface for the rail sample R260. The SEM images showed that there were no visible lamellar structures retained in the subsurface of the wear zone of R260 in the first 60 µm below the surface (Zoom A). Then, there was the co-existence of curved and fragmented cementite lamellae, as underlined with Zoom B. Numerous porosities can be observed and seem to be residual marks of precipitates. EBSD measurements performed in the same area as the SEM images showed a significant loss of Kikuchi patterns for the first 30 µm below the surface. For a depth larger than 30 µm, the nodule structure was completely lost but very small clusters of crystallites sharing similar orientations were perceived: these clusters tended to be very thin (around 1 µm) along ND and elongated (around 5 µm) along the TD.

Figure 7 presents the SEM-EBSD characterization of the microstructure below the worn surface for the rail sample R370CrHT. In the SEM images, contrary to R260, the flattened microstructure was clearly discernible directly below the surface as well as further down the cross-section. A clear tilt of the microstructure was observed: the microstructure realigned itself with the direction of deformation caused by the shearing. As for the EBSD measurements, the loss of Kikuchi patterns occurred at a smaller depth than for R260 (around 5 to 10 µm). A steep gradient of microstructure was perceived: in the first 15 µm, small clusters of crystallites sharing similar orientations were observed, with an increase of these cluster sizes with the increase of the depth of the observation.

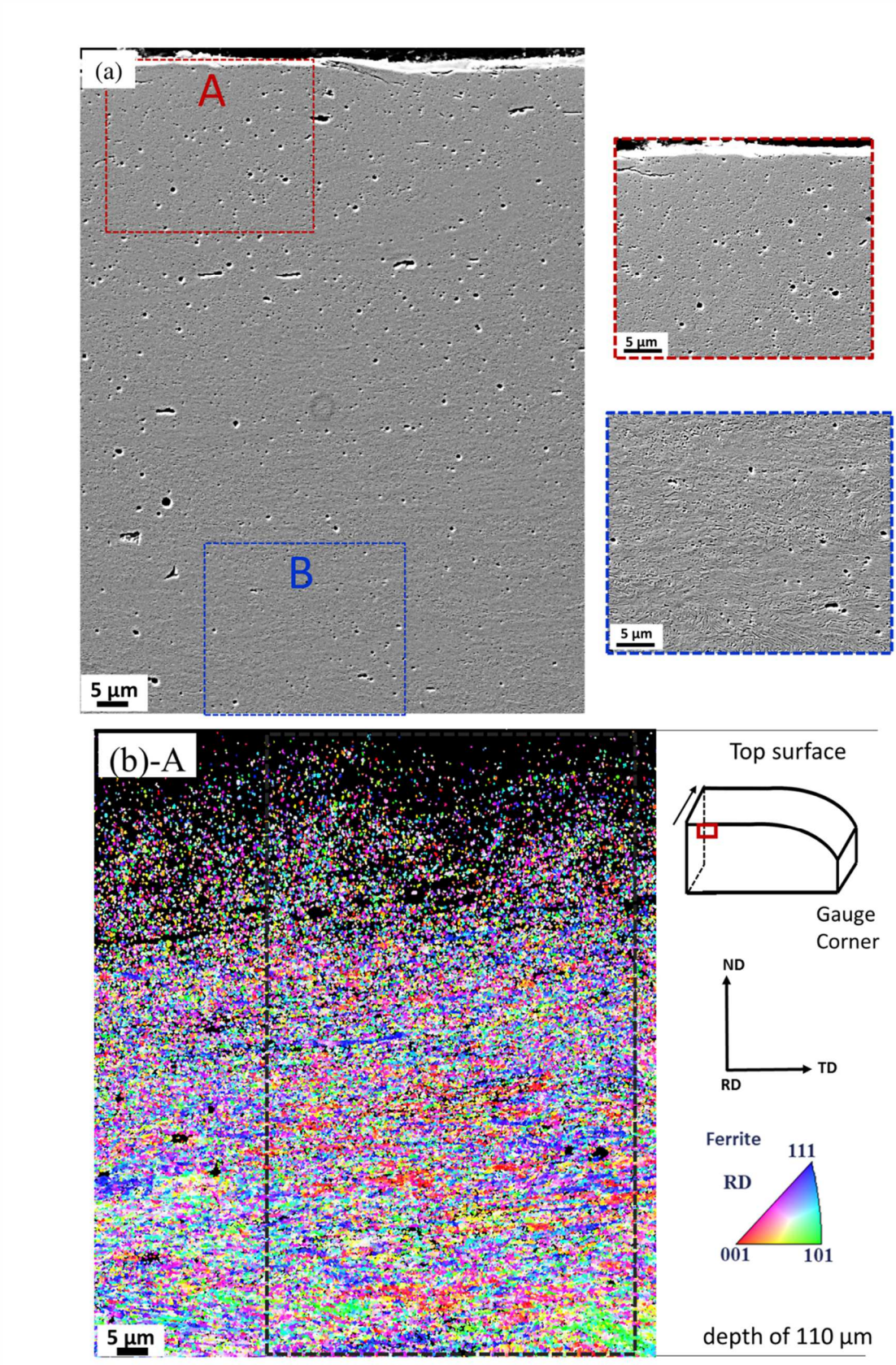

Figure 6: SEM-EBSD observations of the near surface of rail R260 after rig-testing, taken from the cross-section (ND-TD plane), (a) SEM observation and (b) IPF map of the same area.

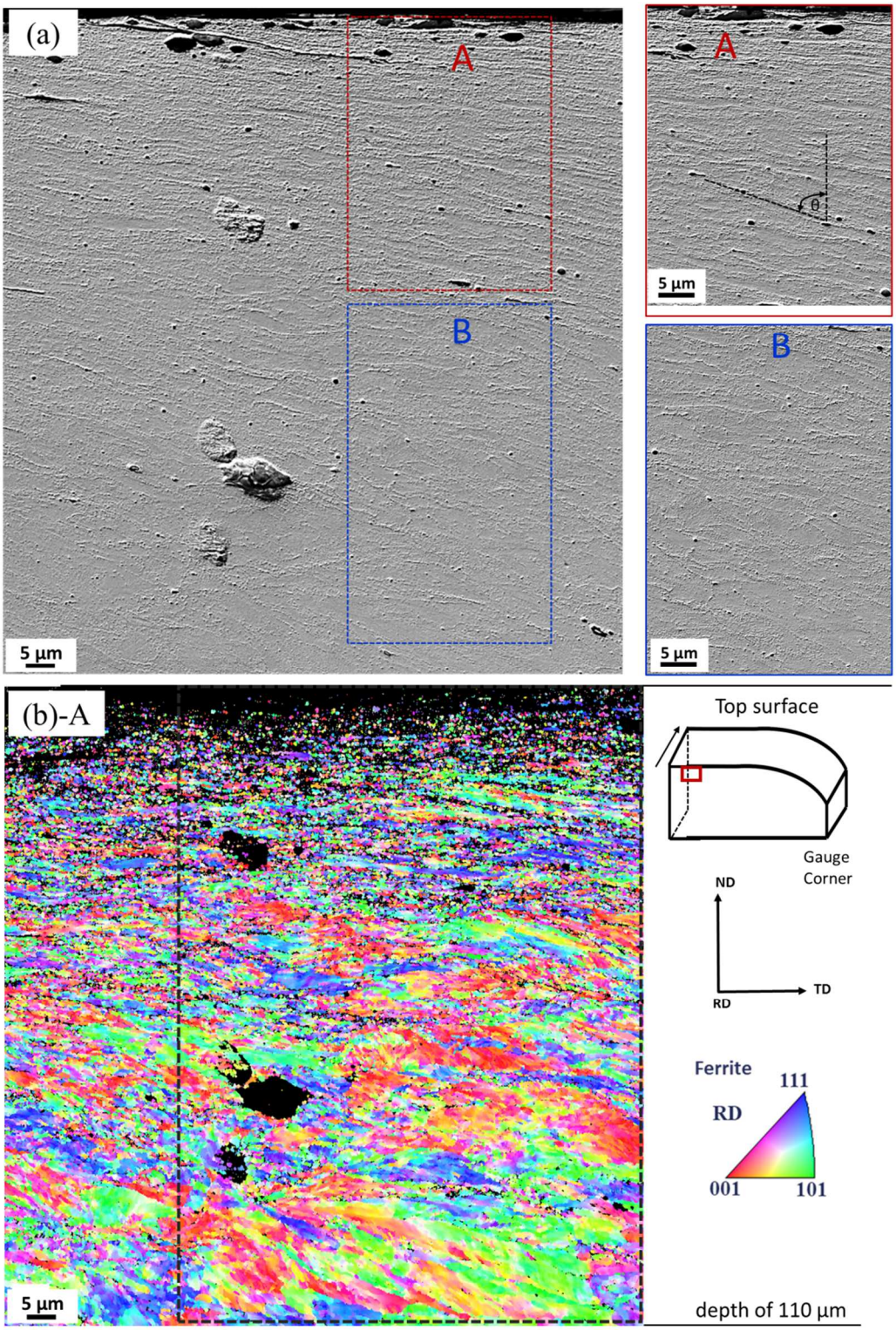

Figure 7: SEM-EBSD observations of the near surface of rail R370CrHT after rig-testing taken from the cross-section (ND-TD plane).

The plastic deformation of the materials caused by the contact between wheel and rail can also be apprehended by visualizing local misorientations. Figure 8 presents the Kernel Average Misorientations (KAM) obtained for R260 and R370CrHT, for the selected zones in the IPF maps of

Figure 6 and Figure 7. Below the worn surface, there was a striking difference in KAM evolutions between the rail sample R260 and R370CrHT. In R260, excluding the non-indexed Kikuchi patterns in the subsurface, KAM between 10° and 65° represented a fraction of 39% of the surface and were distributed all along the examined area. Thus, a considerable number of high-angle boundaries were produced in the near surface. On the opposite, for the same depth, KAM between 10° and 65° represented a fraction of 22% of the surface for R370CrHT. Moreover, a clear gradient was observed in the R370CrHT sample with a decrease of the KAM angles along the depth of the cross-section. Thus, R370CrHT showed a steeper gradient confined to the near surface of the railhead.

These results were checked with the computation of the misorientation angle for the near-surface wear zone in R260 and R370CrHT and were compared with the misorientation angle computed for the near-surface symmetrical areas *i.e.* the unloaded state (Figure 9). The Mackenzie distribution [19] was also drawn as a reference for a cubic sample with a random texture. The distribution of misorientation angle in the symmetrical zone was found to be different from the shown random distribution for both steel grades. It can be explained by the rail production method as well as by the pearlite structure (colony, lamellae) that led to have much LAB than HAB in the considered measurements (as can be observed in Figure 4) and thus caused a distribution that differed from 'standard' grain definition. Then, plastic deformation led to the creation of HAB through the subdivision and rotation of the lamellae and the changes of shape and size of the ferrite grains. More specifically, based on Figure 9, it can be seen that in R260, the number fraction of high misorientation angle was nearly twice higher below the surface in the loaded state compared to the unloaded state. For R370CrHT, the results were completely different: low and high misorientation angles tended to have similar values of number fraction but there was an increase of medium misorientation angles (between 20 and 30 degrees).

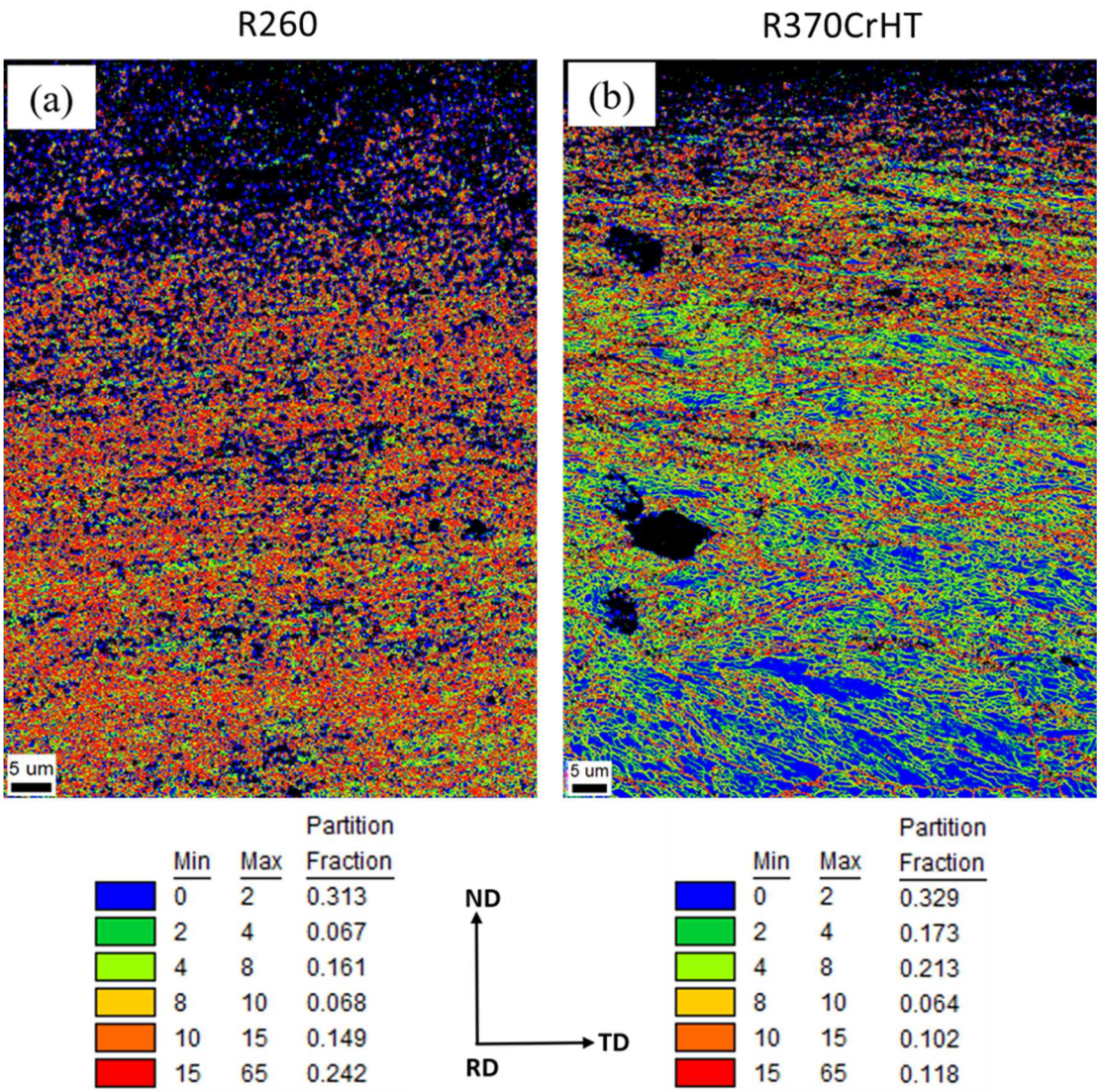

Figure 8: KAM maps corresponding to the selected rectangle in Figure 6 and Figure 7, R260 (a) and R370CrHT (b).

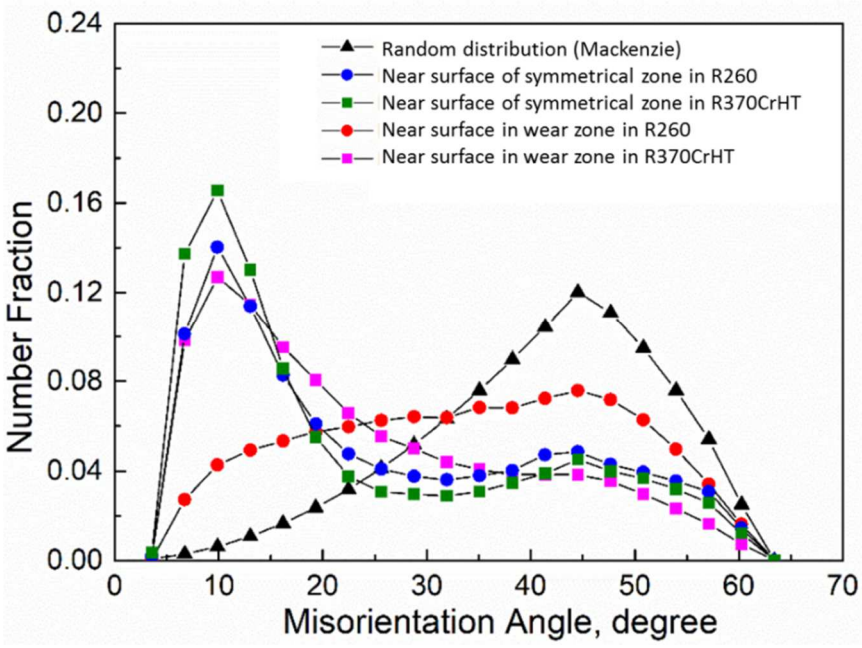

Figure 9: Misorientation angle distribution in the near surface of R260 and R370CrHT.

The microstructure evolution of R260 and R370CrHT was then investigated at different depths below the worn surface using EBSD measurements. Figure 10 and Figure 11 are representative of the EBSD characterizations performed at 150, 500 and 3500 µm in R260 and R370CrHT, respectively. A quick look at the superimposed IQ and rotation angle maps already emphasized the difference of behaviors between R260 and R370CrHT. The red color standing for rotation angles larger than 10° clearly prevailed in the R260 map. More specifically, for R260, the maps combining IPF and IQ suggested a larger interlamellar spacing with the increase of depth, which confirmed the results shown in Figure 5. Contrary to the observations made immediately below the worn surface (Figure 6), larger sub-structures recalling prior-nodules and colonies were observed. However, the disorientations remained too large to try to identify and quantify these substructures. On the combined IQ and rotation angle map, a total length of boundaries equal to 13.7 mm was calculated for the examined depth of 150 µm, composed of 30% of LAB and 70% of HAB. This total length of boundaries progressively decreased along the depth of the sample R260 with a total length of 12.2 mm at 500 µm, with 39% of LAB and 61% of HAB. This decreasing was even larger at a depth of 3500 µm with a total length of 9.9 mm, with 53% of LAB and 47% of HAB. However, the total length of boundaries as well as the fraction of HAB remained much larger than the reference (Figure 4). A non-deformed microstructure was only identified from a depth of 5 mm for R260.

On the opposite, R370CrHT quickly retrieved a microstructure devoid of any plastic markers (at the scale of the EBSD). The EBSD characterizations performed at a depth of 150 µm below the worn surface showed structures very similar to nodules with elongated shapes titled relative to the loading axis (ND). These structures contained some HAB but LAB were dominant. A total length of boundaries equal to 8.7 mm was identified at a depth of 150 µm, with 63% of LAB and 37% of HAB. Then, this total length quickly dropped at a value of 4.1 mm for a depth of 500 µm, with 56% of LAB and 44% of HAB. Finally, the total length of boundaries was equal to 2.7 mm for a depth of 3500 µm, with 64% of LAB and 35% of HAB. It is worth noting that in R370CrHT, even if the total length of boundaries was different along the investigated depths, the ratio of LAB and HAB remained globally unchanged. For R370CrHT, the performed analyses showed that the indicators of plastic activity were confined to a depth of around 700 µm, which is seven times smaller than the value identified for R260. Figure 10 and Figure 11 also showed that in R260, the nodule and colony structures were quickly lost and there were important rotations of lamellae. On the other side, in R370CrHT, colony and nodule structures were largely kept, even when undergoing large deformations. Thus, it seems that in R370CrHT, small interlamellar spacing, combined with small colony and nodule structures, led to the formation of strong cell structures that are more resistant to plastic deformation.

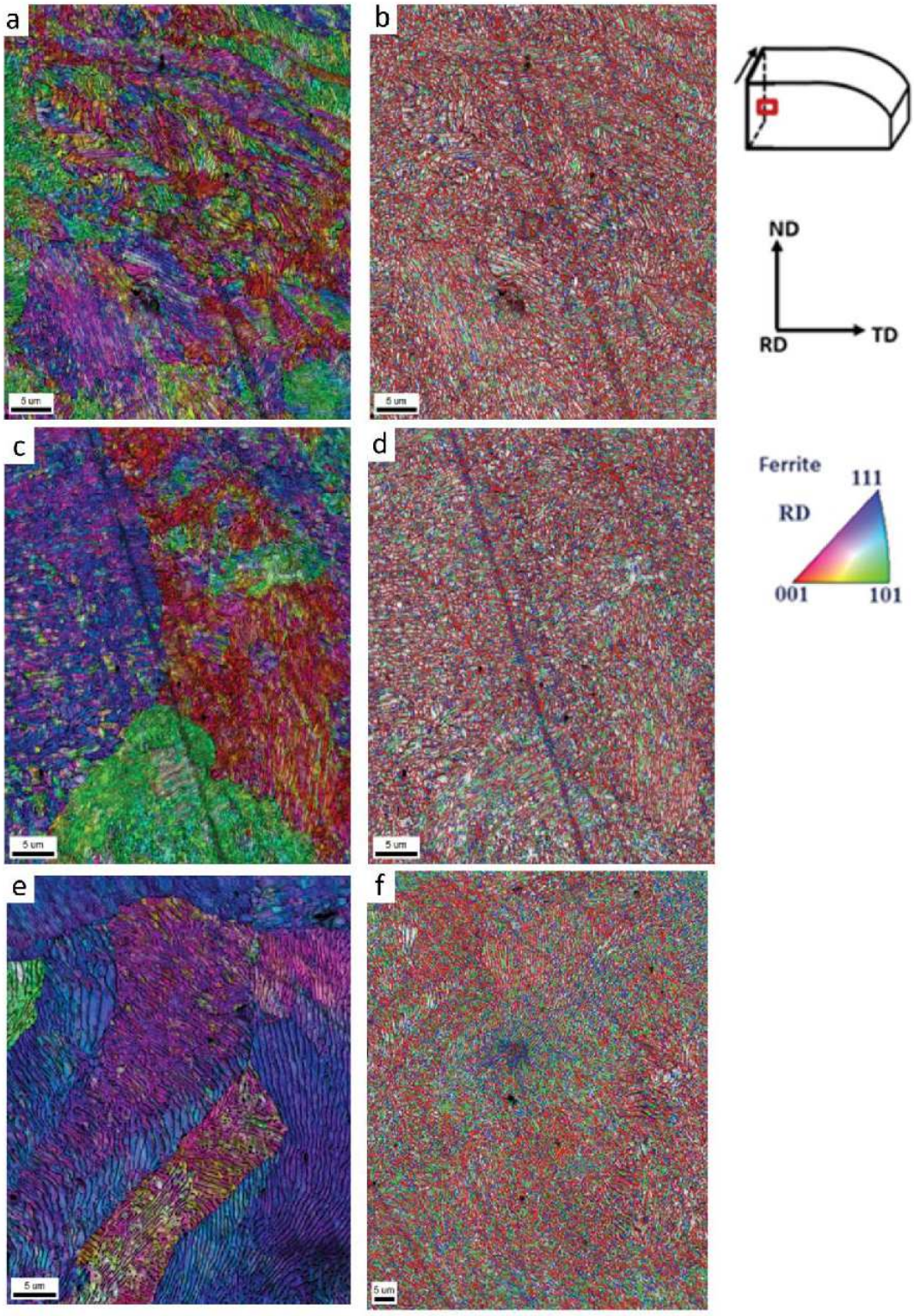

Figure 10: EBSD characterization performed at depths of 150, 500 and 3500 µm in R260: (a), (c), (e) IPF maps superimposed with image quality; (b), (d), (f) IQ map with grain boundaries (2-5° in blue, 5-10° in green, 15-65° in red).

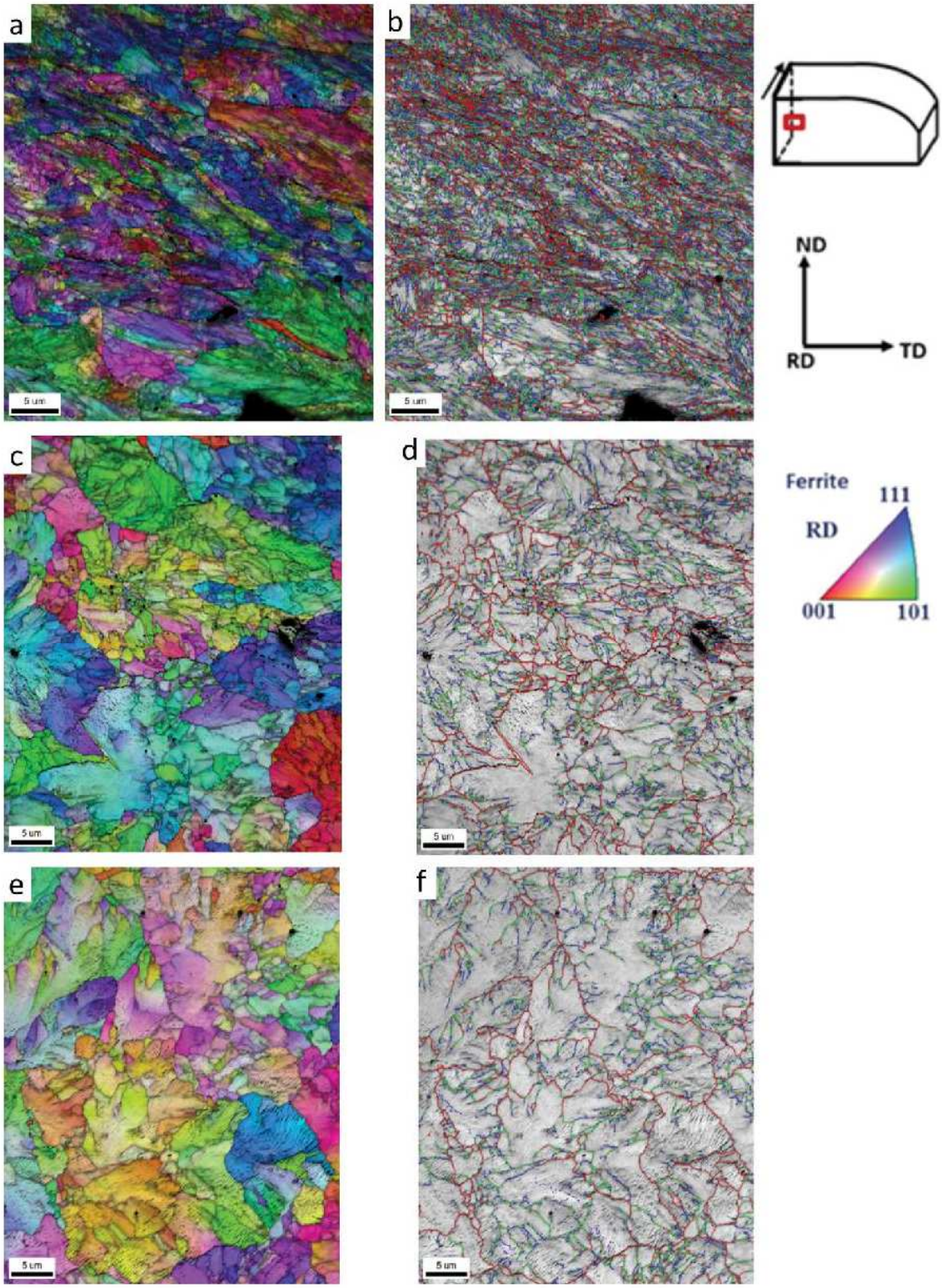

Figure 11: EBSD characterization performed at depths of 150, 500 and 3500 µm in R370CrHT: (a), (c), (e) IPF maps superimposed with image quality; (b), (d), (f) IQ map with grain boundaries (2-5° in blue, 5-10° in green, 15-65° in red).

It should be noted that even if the total load of the rig-tested rails was estimated to be around 2.4 MGT, the large plastic deformations were characteristics of much larger tonnages. The microstructure

characteristics of the examined R260 after deformation were closer to the observations performed by Dylewski *et al.* on a R260 that had supported 350 MGT in real traffic conditions [20] than the observations made on a R260 at the early stages of deformation (1.3 to 16 MGT) [14].

The previous results showed that the deformation behavior of R260 and R370CrHT at the microstructure scale was strikingly different. Figure 12 schematically summarizes the microstructure evolution differences between both steel grades. For R260, directly below the worn surface, there was a complete loss of the microstructure: no colonies, nodules or lamellae were observed. Then, some fragmented and curved lamellae were observed as well as some clusters of crystallites showing similar orientations. In R260, the HAB were so numerous and predominant that the nodule structure could not be identified. Signatures of plastic deformations were found until a depth of approximately 5000 µm. On the contrary, for R370CrHT, the microstructure was still observed directly below the worn surface, even if it was very deformed. Thin and elongated structures tilted relative to the loading direction (ND) were present until a depth of 50 µm. Then, the nodules, even if flattened and tilted, were clearly observed. They quickly regained their round shape with the increase of depth. Signatures of plastic deformations were found until a depth of only 700 µm. Based on these characterizations, it seems that the smaller interlamellar spacing in R370CrHT, combined with smaller structuration (colony, nodule) led to the formation of strong cell structures that are more resistant to plastic deformation, thus slowing down material wear.

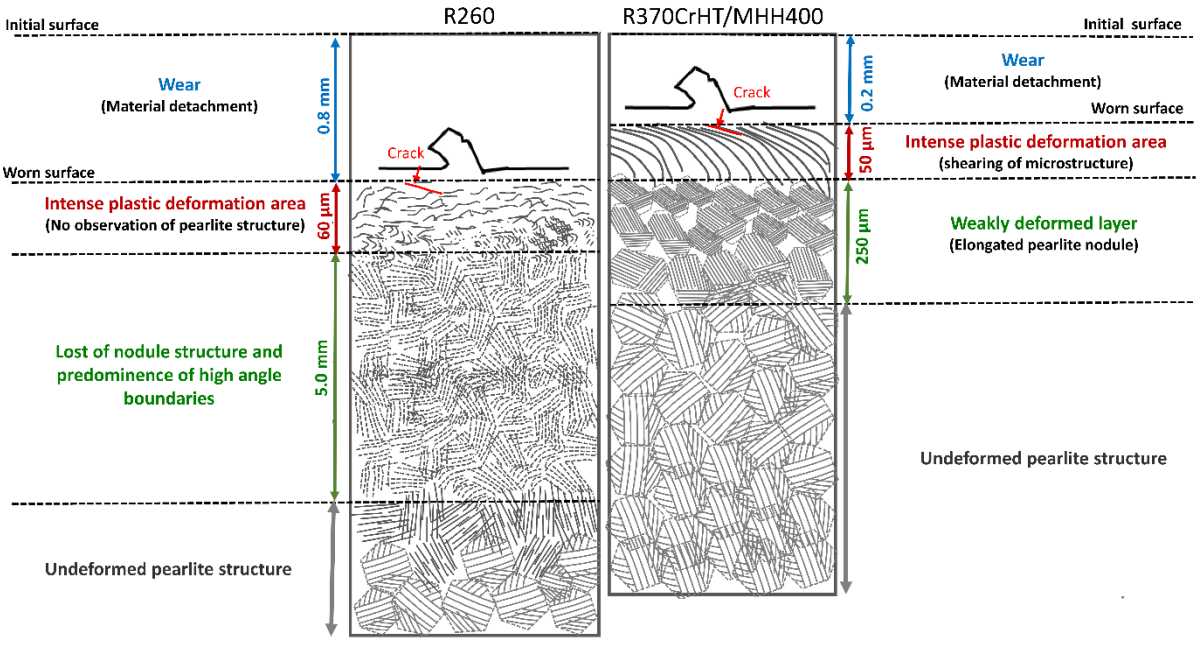

Figure 12: Schematic illustration of microstructure evolution below the worn surface of two rail grades R260 and R370CrHT after rolling contact wheel/rail rig testing.

4. Conclusion

The purpose of this investigation was to examine rail wear in two pearlitic steel: a standard grade (R260) and a heat-treated premium grade (R370CrHT improved to 400 HB). To do so, a full-scale wheel/rail contact rig test was used to reproduce large deformations (loadings around 100 MGT) in a short period of time (computed loadings were equal to 2.4 MGT). Macroscopic observations of worn rails showed that the loss of transverse rail profile caused by the test was more severe in R260 as the wear depth was at least four times larger than the one identified for R370CrHT.

The combination of optical, SEM observations, microhardness tests and EBSD characterization enabled us to explain this difference of wear behavior. The main results of this study are:

- plastic deformation was much more confined in R370CrHT than in R260. The examination of the misorientation angles and rotation angles led to identify microscopic plastic deformation activity until a depth of 5 mm for R260 while this depth was only equal to 700 µm for R370CrHT.
- Stronger strain-hardening was noticed for R260 with an increase of the microhardness at the surface of the material of 60% while it was only 30% for R370CrHT. Moreover, the microhardness varied over a depth of 600 µm for R260 while it decreased over a depth of only 350 µm for R370CrHT.
- The R260 steel rail completely lost its microstructure below the worn surface (absence of colonies, nodules, lamellae) contrary to the R370CrHT steel that kept visible lamellae and had elongated sheared structures tilted relative to the loading axis.
- High angle boundaries were predominant in R260 and prevented any recognition of nodule structuration. On the contrary, nodule structuration was quickly retrieved below the surface in R370CrHT.
- The smaller interlamellar spacing in R370CrHT, compared to R260, combined with smaller structuration (colony, nodule) led to the formation of strong cell structures that are more resistant to plastic deformation, thus slowing down material wear.

This through comparison of the microstructure changes induced in two pearlitic rail steels subjected to a wheel/rail contact rig test will help the building of wear scenarios. Future work will focus on smaller scale to improve the understanding of lamellae deformation.

5. Acknowledgements

The authors would like to thank France Rail Industry, IRT Railenium for their support for this project.

6. References

[1] A.M. Elwazri, P. Wanjara, S. Yue, The effect of microstructural characteristics of pearlite on the mechanical properties of hypereutectoid steel, Mater. Sci. Eng. A. 404 (2005) 91–98. https://doi.org/http://dx.doi.org/10.1016/j.msea.2005.05.051.

[2] P. Clayton, D. Danks, Effect of interlamellar spacing on the wear resistance of eutectoid steels under rolling-sliding conditions, Wear. 135 (1990) 369–389. https://doi.org/http://dx.doi.org/10.1016/0043-1648(90)90037-B.

[3] M. das G.M. da Fonseca Gomes, L.H. de Almeida, L.C.F.C. Gomes, I. Le May, Effects of microstructural parameters on the mechanical properties of eutectoid rail steels, Mater. Charact. 39 (1997) 1–14. https://doi.org/http://dx.doi.org/10.1016/S1044-5803(97)00086-7.

[4] F.A.M. Alwahdi, A. Kapoor, F.J. Franklin, Subsurface microstructural analysis and mechanical properties of pearlitic rail steels in service, Wear. 302 (2013) 1453–1460. https://doi.org/http://dx.doi.org/10.1016/j.wear.2012.12.058.

[5] X.J. Zhao, J. Guo, H.Y. Wang, Z.F. Wen, Q.Y. Liu, G.T. Zhao, W.J. Wang, Effects of decarburization on the wear resistance and damage mechanisms of rail steels subject to contact fatigue, Wear. 364–365 (2016) 130–143. https://doi.org/10.1016/J.WEAR.2016.07.013.

[6] Y. Zhou, S. Wang, T. Wang, Y. Xu, Z. Li, Field and laboratory investigation of the relationship between rail head check and wear in a heavy-haul railway, Wear. 315 (2014) 68–77. https://doi.org/10.1016/J.WEAR.2014.04.004.

[7] K.M. Lee, A.A. Polycarpou, Wear of conventional pearlitic and improved bainitic rail steels,

Wear. 259 (2005) 391–399. https://doi.org/10.1016/J.WEAR.2005.02.058.

[8] N. Larijani, J. Brouzoulis, M. Schilke, M. Ekh, The effect of anisotropy on crack propagation in pearlitic rail steel, Wear. 314 (2014) 57–68. https://doi.org/10.1016/J.WEAR.2013.11.034.

[9] F. Wetscher, R. Stock, R. Pippan, Changes in the mechanical properties of a pearlitic steel due to large shear deformation, Mater. Sci. Eng. A. 445–446 (2007) 237–243. https://doi.org/10.1016/J.MSEA.2006.09.026.

[10] A.C. Athukorala, D. V. De Pellegrin, K.I. Kourousis, Characterisation of head-hardened rail steel in terms of cyclic plasticity response and microstructure for improved material modelling, Wear. 366–367 (2016) 416–424. https://doi.org/10.1016/J.WEAR.2016.03.024.

[11] T. Takahashi, D. Ponge, D. Raabe, Investigation of Orientation Gradients in Pearlite in Hypoeutectoid Steel by use of Orientation Imaging Microscopy, Steel Res. Int. 78 (2007) 38–44. https://doi.org/10.1002/srin.200705857.

[12] J. Debehets, J. Tacq, A. Favache, P. Jacques, J.W. Seo, B. Verlinden, M. Seefeldt, Analysis of the variation in nanohardness of pearlitic steel: Influence of the interplay between ferrite crystal orientation and cementite morphology, Mater. Sci. Eng. A. 616 (2014) 99–106. https://doi.org/10.1016/J.MSEA.2014.08.019.

[13] M. Linz, U. Cihak-Bayr, A. Trausmuth, S. Scheriau, D. Künstner, E. Badisch, EBSD study of early-damaging phenomena in wheel–rail model test, Wear. 342–343 (2015) 13–21. https://doi.org/http://dx.doi.org/10.1016/j.wear.2015.08.004.

[14] B. Dylewski, S. Bouvier, M. Risbet, Multiscale characterization of head check initiation on rails under rolling contact fatigue: Mechanical and microstructure analysis, Wear. 366–367 (2016) 383–391. https://doi.org/10.1016/J.WEAR.2016.06.019.

[15] P. Pointner, High strength rail steels—The importance of material properties in contact mechanics problems, Wear. 265 (2008) 1373–1379. https://doi.org/http://dx.doi.org/10.1016/j.wear.2008.03.015.

[16] European Norm EN 13674-1+A1. Railway applications – track – rail – Part 1: Vignole railway rails 46 kg/m and above., (2017). https://www.boutique.afnor.org/norme/nf-en-13674-1a1/applications-ferroviaires-voie-rails-partie-1-rails-vignole-de-masse-superieure-ou-egale-a-46-kg-m/article/901606/fa189428 (accessed October 31, 2019).

[17] NF EN 13715+A1 - January 2011 - Railway applications - Wheelsets and bogies - Wheels - Tread profile, (n.d.). https://www.boutique.afnor.org/standard/nf-en-13715a1/railway-applications-wheelsets-and-bogies-wheels-tread-profile/article/639918/fa170027 (accessed November 21, 2019).

[18] EDAX/TSL. OIM analysis 5.3 software user manual., (2007).

[19] J.. Mackenzie, Second Paper on the Statistics Associated with the Random Disorientation of Cubes, Biometrika. 45 (1958) 229–240.

[20] B. Dylewski, M. Risbet, S. Bouvier, The tridimensional gradient of microstructure in worn rails – Experimental characterization of plastic deformation accumulated by RCF, Wear. 392–393 (2017) 50–59. https://doi.org/10.1016/J.WEAR.2017.09.001.

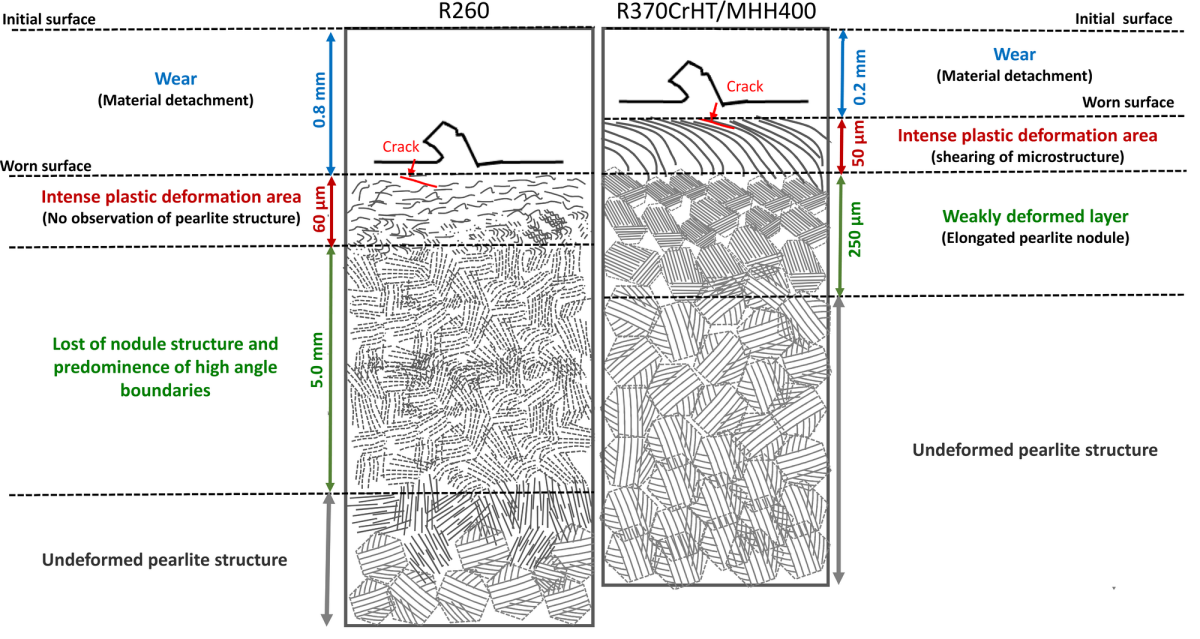
R260
R370CrHT/MHH400
Initial surface
Initial surface
Wear
(Material detachment)
0.8 mm
Crack
Worn surface
Intense plastic deformation area
(No observation of pearlite structure)
60 µm
Lost of nodule structure and
predominence of high angle
boundaries
5.0 mm
Undeformed pearlite structure
Crack
0.2 mm
Wear
(Material detachment)
Worn surface
50 µm
Intense plastic deformation area
(shearing of microstructure)
250 µm
Weakly deformed layer
(Elongated pearlite nodule)
Undeformed pearlite structure